Morphological and nanostructure characteristics of soot particles emitted from a jet-stirred reactor burning aviation fuel

Hu, Xuehuan; Yu, Zhenhong; Chen, Longfei; Huang, Yong; Zhang, Chi; Salehi, Fatemeh; Chen, Rui; Harrison, Roy M.; Xu, Jinglei

DOI:
10.1016/j.combustflame.2021.111760

Document Version
Peer reviewed version

Citation for published version (Harvard):
Hu, X, Yu, Z, Chen, L, Huang, Y, Zhang, C, Salehi, F, Chen, R, Harrison, RM & Xu, J 2022, 'Morphological and nanostructure characteristics of soot particles emitted from a jet-stirred reactor burning aviation fuel', *Combustion and Flame*, vol. 236, 111760. https://doi.org/10.1016/j.combustflame.2021.111760

Morphological and Nanostructure Characteristics of Soot Particles Emitted from a Jet-Stirred Reactor Burning Aviation Fuel

Xuehuan Hu[a,b], Zhenhong Yu[c], Longfei Chen[a, d *], Yong Huang[a], Chi Zhang[e], Fatemeh Salehi[f], Rui Chen[g], Roy M. Harrison[h, i], Jinglei Xu[a, d]

[a] Department of Energy and Power Engineering, Beihang University, Beijing, 100191, China

[b] Department of Atmospheric and Oceanic Sciences, McGill University, Montreal, H3A 0G4, Canada

[c] Hudson River Research, Jersey City, New Jersey, 07310, USA

[d] Beihang Hangzhou Innovation Institute (Yuhang District), Hangzhou, Zhejiang, 310023, China

[e] National Key Laboratory of Science and Technology on Aero-Engine Aero-Thermodynamics, Research Institute of Aero-Engine, Beihang University, Beijing, 100191, China

[f] Department of Mechanical Engineering, Macquarie University, NSW, 2109, Australia

[g] Beijing Key Laboratory of Occupational Safety and Health, Institute of Urban Safety and Environmental Science, Beijing Academy of Science and Technology, Beijing, 100054, China

[h] Department of Geography, Earth & Environmental Sciences, University of Birmingham, Edgbaston, Birmingham, B15 2TT, United Kingdom

[i] Department of Environmental Sciences / Center of Excellence in Environmental Studies, King Abdulaziz University, PO Box 80203, Jeddah, 21589, Saudi Arabia

Highlights

- The increased combustion pressure reduced soot reactivity.
- The low temperature increased the reactivity of soot particles.
- High combustion pressure increased the degree of graphitization.

Abstract: Aircraft engine soot emissions have been a growing concern because of their adverse impacts on global climate and human health. In this study, soot emissions from a Jet-Stirred Reactor (JSR) which could be considered as a basic aero-engine combustor were investigated

* Corresponding author. Email address: chenlongfei@buaa.edu.cn.

under different combustion conditions including varying combustion pressures, fuel flow rates, and inlet air temperatures. The emitted soot particles were collected onto quartz fiber filters and then examined using high-resolution transmission electron microscopic (HRTEM) and Raman techniques. The HRTEM images and Raman spectra of the filter-laden soot samples were analyzed to determine the morphology and the nanostructure characteristics of the soot particles. It turned out that compared to the reference point, both high combustion pressure and high flow rate led to an increase in primary particle size. The HRTEM and Raman studies showed that there was no amorphous carbon present in the soot particles generated under high combustion pressure. Inlet air temperature exhibited a significant influence on the size and the morphology of soot particles; a large quantity of amorphous carbon with a lower degree of graphitization was generated under the low inlet temperature condition presumably due to poor fuel spray breakup and atomization in the JSR. In addition, we found that nanostructure parameters, such as soot fringe length and fringe tortuosity could be strongly dependent upon the residence time and the inlet air temperature.

Keywords: Jet-Stirred Reactor; soot particle emissions; particle size distributions; fringe parameters; Raman spectra.

1. Introduction

There is an increasing concern about soot particles emitted from aircraft engines because of their adverse impact on air quality and human health [1, 2] and upon climate. Therefore, aviation soot emissions are limited by law in the International Civil Aviation Organization (ICAO) Committee. For turbofan/turbojet engines, a new ICAO Standard and Recommended Practice (SARP) on non-volatile particulate matter (nvPM) number and mass emissions have been approved and will be put into effect from 1 January 2023 [3]. The past regulation only mandated smoke number

measurement, which suffers low sensitivity and is no longer a suitable metric for regulating modern low-emission aero-engines.

As the only direct soot emission source in the upper troposphere and lower stratosphere, the soot particles emitted from aircraft engines can interact with other ambient chemical constituents including water vapor and trigger contrails and cirrus clouds formation [4], and thus influence solar radiation and aqueous vapor distribution at cruise altitudes as well as affect global climate patterns [5, 6]. A previous study demonstrated that aviation-induced contrails and cirrus clouds may even have a greater contribution to global radiative forcing than that from aviation CO_2 emission[7], yet this area has not received much attention. A recent study of contrail formation mechanism has found that the oxidation of aviation soot particles significantly enhances soot activation (ratio between the number of the nucleated droplets and seeding particles), regardless of the sulfur present in the fuel [8]. The key characteristic of soot oxidation has received increasing attention [9, 10]. There have been many studies on the topic of the oxidation of soot particles, including the critical influence of soot morphology and nanostructures [9, 11]. Nanostructure characteristics such as fringe length and fringe tortuosity can characterize the spacing and scale of graphene layers in primary soot particles, and may be used as an indicator of oxidation potential [11].

The existing investigation on the oxidation properties of soot particles has mainly focussed on soot emissions from diesel and gasoline engines [12, 13], which are dramatically different from aircraft gas turbine engines due to the difference in fuel composition, engine operational principle and combustion conditions. For instance, the size of soot particles emitted from modern aircraft engines is normally noticeably smaller than the soot particles emitted from diesel and gasoline

engines [14]. Therefore, detailed investigations of oxidation and the related morphology and nanostructures of aviation soot particles could provide important information for the understanding of contrail formation from aviation activities and their potentially significant impact on climate.

The operating conditions of aircraft engines are critical for soot formation and oxidation [15, 16] because the physical and chemical properties of soot particles are closely related to combustion conditions. Previous studies on soot particles from aircraft engines have provided valuable information and first-hand data [17, 18]. However, aircraft engine tests are normally very expensive and may only quantify the effect of engine operational parameters (such as engine power and speed) on the formation of soot particles, yet the fundamental effects of relevant thermodynamic parameters (such as combustion temperature and pressure) on soot formation cannot be evaluated [14, 19]. Liati et al. [18] demonstrated that primary soot particles generated under full power conditions were the largest in size among their tests (> 24 nm), but exhibited the lowest capacity for oxidation. Huang and co-workers [17] reported that the morphology of primary soot particles shifted from shell-amorphous to graphitic-like shape as engine power increased. To evaluate the relationship between the physical combustion parameters and soot characteristics, a more fundamental investigation is needed to eliminate inevitable variations in soot emissions associated with engine combustion variability. Using the well-controlled jet-stirred reactor (JSR) [20], which is typically regarded as the fundamental combustor of aero-engines, one can obtain stable soot emissions, and the combustion parameters such as inlet air temperature, combustion pressure, and fuel flow rate ratio can be easily controlled with little variation [21, 22]. Compared with aero-engine tests or combustor tests, a JSR could be a more economical and practical instrument to investigate the characteristics of aviation soot particles.

In this study, the soot emissions from a JSR representing an aircraft engine combustor were characterized via a high-resolution transmission electron microscope (HRTEM) and a Raman spectroscopy. HRTEM is a well-established technique to obtain the morphology and the nanostructure of soot particles [23]. Raman spectroscopy is used to analyze the nanostructure of soot [24-27]. Since Raman spectra are sensitive to the graphite structures and crystal defects of soot particles, the graphitization order of soot particles can be determined by using Raman spectroscopic analysis [24-26, 28]. The effects of combustion pressure, fuel flow rate, and inlet air temperature on soot characteristics were comprehensively investigated. We aimed to assess which fundamental combustion parameters change the soot nanostructure and thus influence the soot reactivity or oxidation potential. Traditionally, oxidation reactivity of combustion soot has also been examined by thermogravimetric analysis (TGA) approaches [29], but in this study, we would focus on the impacts of soot nanostructures on its reactivity. The results of this study could provide the reference for developing strategies for decreasing aviation soot emissions and altering their morphology and nanostructures to mitigate contrail formation.

2. Experimental

2.1. Test Facilities and Sampling Conditions

The tested jet-stirred reactor in this study has only one combustion stage (diffusion combustion stage), which is different from most modern gas turbine aircraft engines. The selected combustion conditions such as temperature, pressure, and equivalence ratio were not identical to those of real-world applications. For instance, the equivalence ratio was in rich-burn condition to simulate the primary zone combustion of real engines. Because the soot formation is sensitive to combustion temperature, our inlet combustion temperatures were selected to close to the idle condition (4-7%

thrust) of real turbofan engines, while the pressures were slightly less than real ones.

Figure 1 shows the experimental setup for sampling and characterizing soot particles emitted from a JSR, including the combustion system, the diluting/sampling system, and the nanoparticle measurement instruments for offline analysis. The JSR test rig can operate under a wide range of conditions in fuel flow rate (1-1.5 g/s), combustion pressure (1-2 bar) and inlet temperature (360-450°C).

An ignition electrode and thermocouples were used to measure the internal temperatures of the reactor. The sampling probe was 3 mm away from the combustion reactor wall, which did not affect the combustion and the subsequent soot generation. Detailed information about the JSR was provided in the previous publication [30]. The capillary outlet was located in the constricted part of the air channel (1 mm in diameter). The air velocity ranged from 200 to 350 m/s. Both air and fuel were heated before entering the mixing chamber to achieve better evaporation. The residence time is the average time the gas flows and stays inside the combustor and is considered to be one of the most important parameters for determining the combustion and emission characteristics of the commercial gas turbine combustor [20]. The combination of smaller volumes and larger nozzle diameters allowed higher fuel flow rates and shorter residence times.

In order to monitor the combustion operation of the entire JSR system, a series of thermocouples were used in the air loop, the fuel loop, the mixing chamber, and the reactor body. In addition, pressure sensors were also deployed in the air loop and the outlet of the reactor body. The impacts of combustion pressure, inlet flow rate and inlet temperature on soot formation at a equivalence ratio $\phi = 1.2$ were studied. Nitrogen carrier gas can avoid the oxidation of the soot particles and is used to dilute exhaust directly. Then the diluted gas meets cold compressed particle-free air in the dilutor as the second stage to cool down the gas. The internal space of the dilutor is large enough

to mitigate flow turbulence effect. Thus, a uniform aerosol distribution was formed at the exit plane of the dilutor. As shown in Table 1, four test points were measured, namely Reference Point, High Pressure Point, High Flow Rate Point, and Low Inlet Temperature Point. These test points were selected based on the conditions available to the JSR. The low fuel flow rate and high inlet temperature test points were not suitable for this experiment because they would cause unstable combustion.

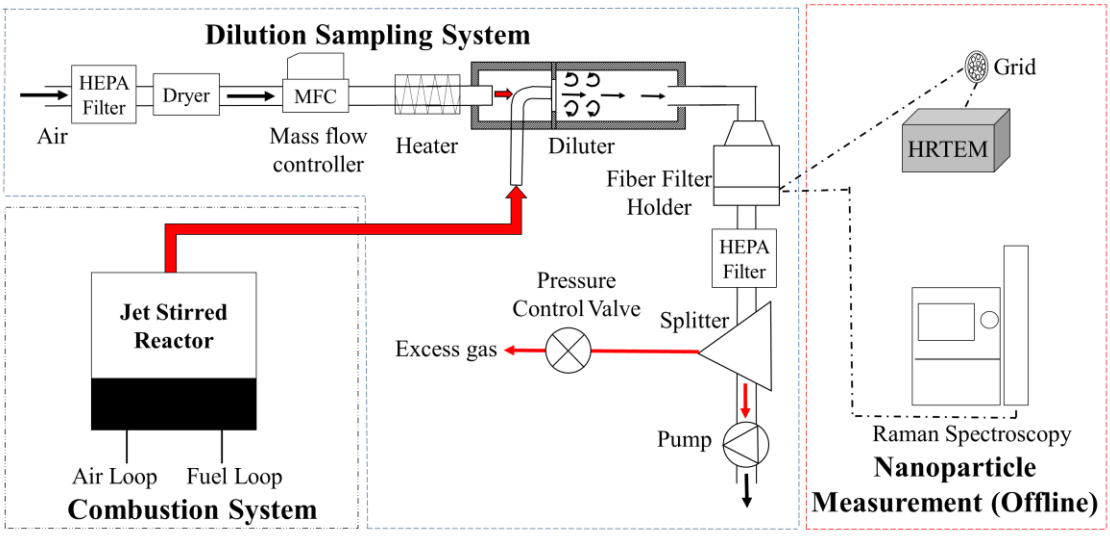

Figure 1. Illustration of the JSR test rig system.

The offline particle analysis systems included a high-resolution transmission electron microscope (HRTEM) and a Raman microscope with laser excitation at 633 nm. Before collecting soot particles on quartz fiber filters, heating equipment and dilution systems were deployed to reduce water condensation and particle thermophoresis losses. The temperature of the transfer line was kept at 190±5°C. During the entire study, the dilution air flow rate was maintained at 10 L/min (lpm) and the dilution ratio was kept at (50 ± 5): 1. So the JSR exhaust flow rate was around 200 mL/min. Soot particles were collected from the subsequent sampler (the quartz fiber filters, GE Whatman, 47 mm), and the collected quartz fiber filters were stored in a refrigerator at

-20°C to prevent it from being oxidized for further offline analysis.

Table 1 Operational parameters of the JSR system.

JSR operational conditions	Reference Point	High Pressure Point	High Flow Rate Point	Low Inlet Temperature Point
Pressure (bar)	1.2	2.0	1.2	1.2
Inlet Temperature (°C)	430	430	430	360
Total Flow Rate (g/s)	1.0	1.0	1.5	1.0
Outlet Temperature (°C)	590 - 1100	605 - 1130	582 – 1070	500 - 880

The test fuel was Chinese aviation kerosene fuel (RP-3, GB6537-2006), and its main specification properties are listed in Table 2. In a previous study, Mao et al. compared the RP-3 fuel and the Jet A fuel [31] in chemical composition. They found that the iso-alkane content in RP-3 was 42.9%, higher than that of 29% in Jet A [32]. The RP-3 fuel used in this study has an H content of 14.5% in mass, similar to those of the 50/50 blends of the JP-8 and Fischer-Tropsch fuels (14.3% and 14.5%) used in the NASA Alternative Aviation Fuel Experiment (AAFAX) [33]. A systematic investigation by Lobo et al. [34] on non-volatile particulate matter (nvPM) emissions from an aircraft auxiliary power unit burning 16 different blends of fuels, has demonstrated that the H content of the fuels correlated with the nvPM emissions, as the reduction of nvPM was greater with increasing H content [35].

The fuel/air equivalence ratio, ϕ, was defined as the ratio of the actual fuel/air ratio to the stoichiometric fuel/air ratio. When ϕ is greater than 1, it indicates fuel-rich and globally incomplete combustion. In this study, ϕ was kept at 1.2 to maintain stable soot emissions. For each test point, the sampling time was fixed at 5 minutes, and three repeatability tests were performed for uncertainty analysis. All the results are listed in Table S1.

Table 2 Fuel properties of the RP-3 fuels.

Fuel Types	RP-3
Chemical Formula	$C_{10.35}H_{20.83}$
Viscosity (mm^2/s)	1.28
Density (g/cm^3)	0.79
Cetane Number	42.00
Lower Heating Value (MJ/kg)	43.43
Oxygen Content (wt%)	0.00
Surface Tension (10^{-3} nm^{-1})	23.60
Sulphur (%)	0.30
Boiling Point (°C)	T10=172.8
	T50=194.9
	T90=224.4

2.2. HRTEM and Raman instruments

A field emission electron microscope (JEM-2100F, JEOL) with an operating voltage of 200 keV and point resolution of 0.23 nm was used to obtain the HRTEM images for offline analysis of soot nanostructures [36]. Soot particles were collected by HRTEM grids (20-nm-thick carbon lacey coated Cu grids, Spi Supplies). Five grids were glued and distributed at different positions on each quartz fiber, as shown in Figure 1. The initial HRTEM images were processed using the open-source ImageJ software, which is a Java-based image processing program [37], to obtain the primary particle diameters by capturing the outlines of spherical-like particles. The nanostructure parameters such as fringe length and fringe tortuosity were then extracted from the HRTEM-derived images using a MATLAB-based code with the algorithm proposed by Yehliu et al. [38]. The fringe length was defined as the straight length of the carbon sheet layers of the primary particle, and the fringe tortuosity was defined as the ratio of the fringe length and fringe distance connecting two fringe endpoints [39]. A schematic of these two nanostructure parameters was also presented in a previous publication [40]. The detailed steps can be found in Figure S1.

The Raman microscope used in this study was Model LabRAM HR 800 from HORIBA, which

measured the Raman spectra from the soot samples deposited on the quartz fiber filters and provided spectroscopic analyzes of the obtained spectra. The detailed measurement and analysis method of the Raman microscope was explained elsewhere in literature [40]. To avoid overheating soot samples, a low laser power of 1.36 mW at 633 nm was applied. All the obtained Raman spectra were processed by the embedded "Lebspec5" software of the instrument, and only the first-order Raman bands less than 2000 cm^{-1} were analyzed.

3. Results and Discussion

3.1. HRTEM results

3.1.1 Particle morphology and primary soot particle size distributions

Figure 2 shows the HRTEM images of the soot particles emitted from the JSR at each test point. These images display the clear morphology of different soot samples. Primary particle diameters were determined by fitting circles to each spherule in the aggregated particles. The HRTEM analyses of particle size distributions were conducted by calculating size-resolved cumulative number-based distributions of the primary particles and converting them into relative abundance (The size distributions normalized by the total numbers of primary particles). In the analyzes, the summarized number concentration at each test point was normalized to unity and the determined particle size distributions (PSD) in relative abundance are shown in Figure 3.

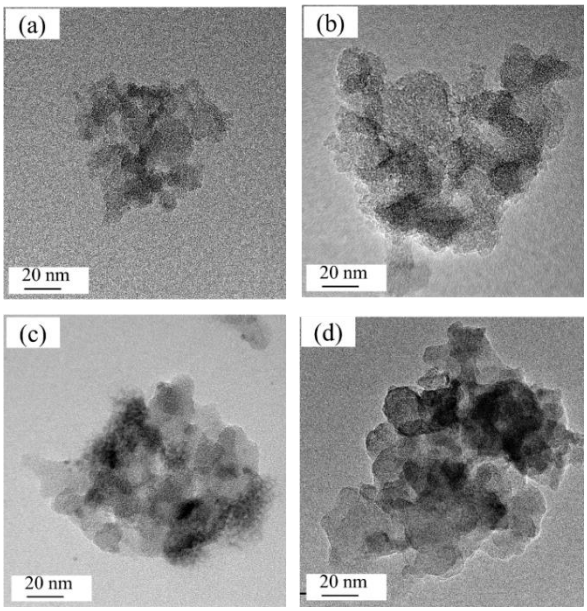

Figure 2. The HRTEM images of soot particles emitted from the JSR at (a) Reference Point, (b) High Pressure Point, (c) High Flow Rate Point, (d) Low Inlet Temperature Point.

The primary soot particles from the JSR at the four test points show significantly different PSDs as illustrated in Figure 3. First, the primary particles at the High Pressure Point are larger than those at the Reference Point, indicating that the high combustion pressure could decrease the residence time, allowing less oxidation of the primary soot particles and eventually resulting in an increase in particle size. The elevated combustion pressure enhances air/fuel mixture preparation and thus may squeeze the main combustion zone where the air/fuel mixture is burned. Given the constant size of the combustor, the post-combustion zone would be expanded to promote the post-oxidation of soot particles, and thus decreasing residence time in the combustion zone; Second, the primary particles at the High Flow Rate Point are larger than those at the Reference Point, presumably because of the short residence time that causes less oxidation of soot particles; Third, the mean diameter of the soot particles at the Low Inlet Temperature Point is 9.8 ± 3.6 nm, compared to 14.2 ± 4.6 nm at the Reference Point, 17.4 ± 4.6 nm at the High Pressure Point, and

20.1 ± 4.9 nm at the High Flow Point. We believe that the smallest soot particle size at the Low Inlet Temperature Point is due to the insufficient inlet temperature exacerbating fuel spray atomization and thus combustion quality in the reactor. In previous studies, it has been found that low inlet temperature could lead to the release of less heat from fuel oxidation as well as a lower combustion temperature, thus make the soot formation difficult [41-44].

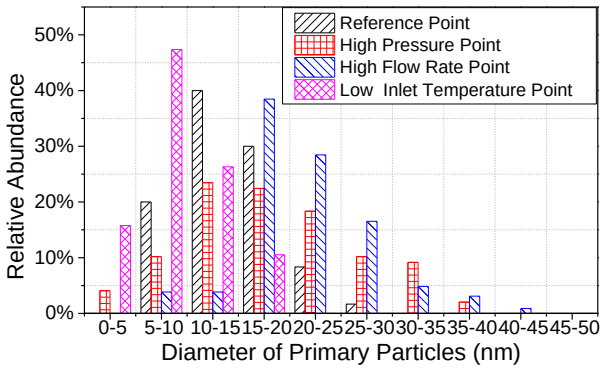

Figure 3. Primary soot particle size distributions in relative abundance derived from HRTEM images.

3.1.2. Particle nanostructures

In this study, at least 50 primary particles for each condition point were analyzed to obtain the statistics. The fringe length and fringe tortuosity are two of the most important nanostructure parameters of soot particles and reflect their oxidation activity during combustion [9, 45]. The fringe length has been found inversely proportional to fringe tortuosity in many studies [9, 45]. Soot particles usually present lower reactivity with longer fringe length and the lower fringe tortuosity [9]. Particles with longer fringe length tend to have more graphitic structures because there exist fewer edged carbons and reacting with adjacent layers becomes difficult [9]. Lower fringe tortuosity means that there exist fewer curved graphene segments and larger bonding forces among carbon atoms, inhibiting their oxidation [9].

The distribution histograms of the fringe length at the four test points are presented in Figure 4. Given the spatial resolution of the HRTEM being 0.23 nm, we omitted the fringes with the length of less than 0.5 nm and the tortuosity of less than 0.5. In this study, we did not choose the 0.5 nm cut-off arbitrarily. Some previous fringe parameter studies for soot particles have shown that the fringe length shorter than 0.483 nm (two aromatic rings or naphthalene) has to be discarded as unrealistic [46, 47]. In other literatures[38, 48], the size distributions of the fringe length are similar to ours. Their analyses also removed the fringe length less than 0.5 nm because it is difficult to distinguish them from noises or non-crystalline structures. The phenomena that the peaks of the fringe length distributions locate at the minimum measured fringe have also been observed in other references [38, 48, 49]. As shown in Figure 4, the fringe lengths of the primary soot particles at each test point are in the range of 0.5 - 4.0 nm, with more than 98% between 0.5 - 2 nm, consistent with a previous study of aero-engine soot particles [50]. The portion of fringe lengths longer than 1.0 nm at the High Pressure Point is slightly larger than that at the Reference Point, while that at the Low Inlet Temperature Point is less than that at the Reference Point. The greater fringe lengths indicate that the soot particles at the High Pressure Point tend to be more graphitic and are more resistant to be oxidized. The shorter fringe length at the Low Inlet Temperature Point implies that primary soot particles emitted under this combustion condition are characterized by the amorphous structure of short fringe length, causing less ordered graphene layer a and higher oxidation potential due to more edge-site carbon atoms [51]. The fringe length data are provided in Table S2.

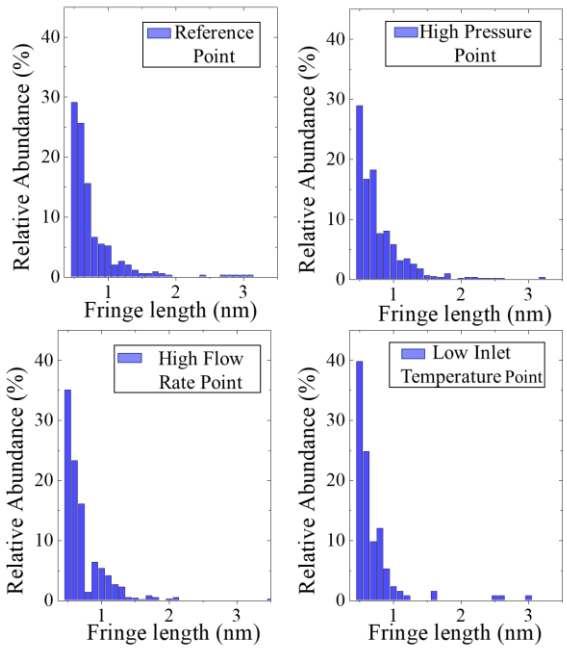

Figure 4. The fringe length distributions (by frequency metric on element counting) of the primary particles under JSR fuel-rich combustion conditions (Fringe lengths above 3.5 nm are not involved here in order to facilitate the axis fitting).

As shown in Figure 5, the fringe tortuosity values of the primary soot particles at the four test points are distributed between 1.0 - 2.0. The fringe tortuosity analysis is presented in Table S3. Curve fitting with the Lorentz functions was applied to the results, as shown as the red lines in Figure.5, to determine the mean value of fringe tortuosity for each condition point. These tortuosity results are in agreement with the previously observed morphology [52, 53]. For instance, the particles at the High Pressure Point exhibit a mean fringe tortuosity of 1.22 ± 0.02 compared to that of 1.28 ± 0.02 at the Reference Point. The smaller fringe tortuosity indicates that the primary soot particles are more mature, with carbon lattices being arranged more tightly, which is associated with high combustion pressure condition. In contrast, the mean fringe tortuosity at the High Flow Rate Point and at the Low Inlet Temperature point is 1.30 ± 0.02 and 1.32 ± 0.02

respectively, higher than that of 1.28 ± 0.02 at the Reference Point. The larger tortuosity at the High Flow Rate Point implies that the primary soot particles have disordered lattices with stronger soot reactivity due to insufficient combustion and short residence time, while the largest fringe tortuosity at the Low Inlet Temperature Point indicates that the low inlet temperature promotes the formation of soot particles with increased reactivity, which presumably because that the soot particles generated under low temperature combustion are less mature than those under high temperature [51].

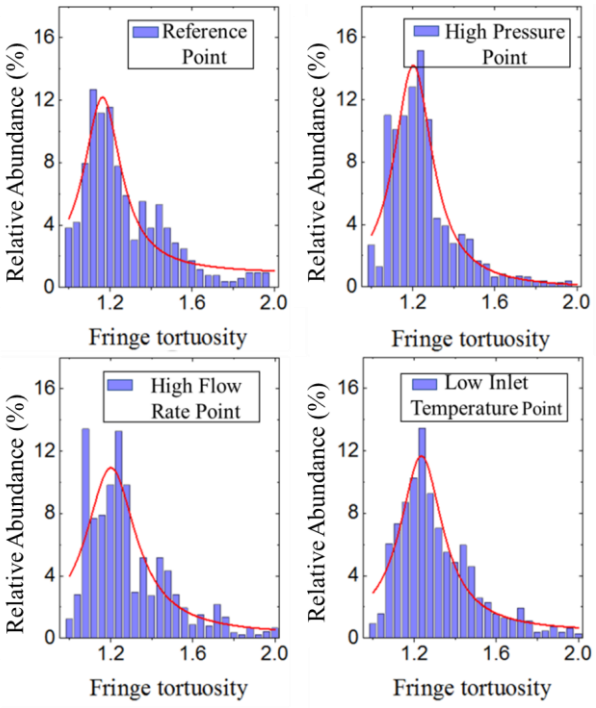

Figure 5. The fringe tortuosity distributions (by frequency metric on element counting) of the primary particles under JSR fuel-rich combustion condition (The fringe tortuosity above 0.7 are not involved here in order to facilitate the axis fitting).

Owing to its high spatial resolution, the HRTEM technique enables the direct observation of nanostructures of primary soot particles [54, 55]. Selected portions of the HRTEM images at each test point are shown in Figure 6. The differences among these HRTEM images demonstrate that

the nanostructures of the soot particles strongly depend on the combustion conditions like temperature, pressure, and the flow rate of fuel/air mixture. For instance, at the High Pressure Point, the soot particles were found to have no hollow interiors, similar to the soot particles from a CFM56-2-C1 engine at 30% thrust, observed by Vander Wal et al. [39]. This observation is consistent with the following Raman analysis that there is no amorphous carbon present in the soot particles at the High Pressure Point. On the other hand, hollow interiors were clearly observed in the soot particles at the Low Inlet Temperature Point and the High Flow Rate Point.

At each test point, the nanostructures of the soot particles feature a single core or multi-cores with short carbon segments (called 'cores') and an outer shell with carbon fringes. Zhang and Kook have found from a nanostructure study on diesel engine soot, that the cores have higher reactivity than the outer shell of primary soot particles because the cores have much shorter carbon fringes, indicating less organized carbon structures [56]. Different nano-structural characteristics are evident in the samples, including 'onion-like,' and 'shell-core' types [51]. The primary soot particles in this study all exhibit 'shell-core' nanostructures as shown in Figure 6, with the graphitized outer shell and many inner cores, indicating more degree of graphite and higher oxidation resistance [57]. This nano-structure type is significantly different from the 'onion-like' and 'shell-core' observed in primary particles emitted from diesel engines [51], which further reinforces the hypothesis that the difference of combustion conditions between aero-engines and diesel engines would cause a significant difference in terms of soot nano-structures and thus soot reactivity.

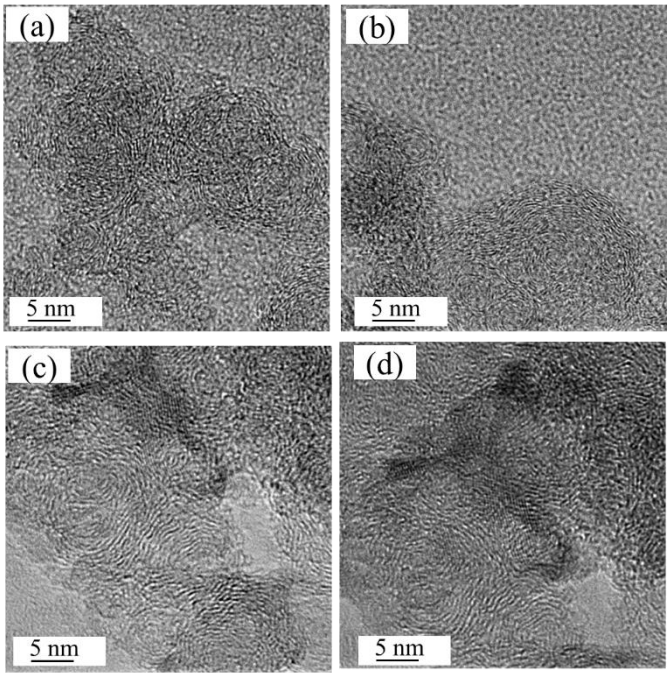

Figure 6. Nano-structures revealed by HRTEM images of representative soot particles at (a) Reference Point, (b) High Pressure Point, (c) High Flow Rate Point, and (d) Low Inlet Temperature Point.

Our study demonstrates that an increase in combustion pressure can result in lower fringe length and larger fringe tortuosity for the soot primary particles, contrary to the effect of lower combustion temperature. There are many studies focusing on engine load, which is related to combustion pressure. Verma et al. [58] found that increasing engine load from 25% to 100% with higher pressure can cause more orderly internal structures of emitted soot particles. Zhu et al. [59] reported that higher engine loads can increase stable nanostructure and less disorder graphitic structures with high combustion temperature at high engine pressure.

However, some studies of diesel engines showed different observations for the nanostructure of soot particles at high engine load. Ye et al. [60] found that high combustion pressure can produce more disordered nanostructure. Hence, the residence time may be another key variable in

determining the soot nano-structures. The longer residence time prolongs the surface growth of the soot particles, thus forming ordered graphite structures [60]. Furthermore, higher combustion temperature can also cause the soot emissions to break down into more small substances, such as C_2H_2 [61], which favor the formation of ordered graphitic structures. Although diesel engine and jet combustors operate under very different conditions, these results can correlate with our observations that higher pressure and longer residence time can have larger fringe length with more orderly nanostructures, while lower inlet temperature promotes the generation of amorphous carbon and the formation of less ordered nanostructures.

3.2 Raman spectra

Raman spectroscopy has been used to analyze the microcrystalline and molecular structures of primary soot particles [62-65]. For ideal single-crystal graphite with few defects or disordered graphitic lattice, only one fundamental band called the G band, which corresponds to the graphitic vibration with E_{2g} symmetry, could be present at 1580 cm^{-1} in the Raman spectrum [26, 28, 66]. However, the soot particles sampled from the JSR in this study were not ideal graphite which had many defects and structural disorders. We observed another four other bands (D1, D2, D3, D4) that represent the defects generated by nanostructures in the soot particles in all the Raman spectra, in agreement with other Raman studies [62, 67]. According to previous soot studies, the D1 band at 1350 cm^{-1} represents a disordered graphitic lattice in A_{1g} symmetry [26, 28, 66] ; the D2 band at 1620 cm^{-1} is associated with a disordered graphitic lattice in E_{2g} symmetry [27, 66]; the D3 band at 1500 cm^{-1} is closely related to amorphous carbon content [62, 68]; and the D4 band at 1200 cm^{-1} has a relationship with sp^2- and sp^3-hybridized carbon bonds and ionic impurities [69, 70].

To quantitatively compare the relevant Raman intensities for each band, we determined the band areas via spectral fitting and then normalized the total areas of the four bands to unity for each test

point. As shown in Figure 7, we found that at each test point, the area of the D1 band is the largest among the four bands indicating that the majority of the elemental carbon inside the soot particles is disordered. Similar to a previous Raman investigation on soot emissions from several commercial gas turbine engines [71], our results indicate that the D1 band contributes the most to the total D and G Raman intensities for aviation soot particles. The G band has a similar area value at each test point, which implies that the ordered graphitic contents are nearly the same for the soot particles generated at each test condition. Since there is no D3 band observed at the High Pressure Point, the nano-structures of the soot particles under this condition may contain little amorphous carbon, implying that at the high-pressure more mature soot particles were produced, but the majority of the graphitic carbon content is disordered, consistent with the observation of the highest contribution from the D1 band. At the Low Inlet Temperature Point, the contribution of the D1 band is the smallest and that of the D3 band is the highest among the four test points. This indicates that in the soot particles generated under the low inlet temperature condition, there is the most amorphous carbons and the fewest defects at the edges of the graphitic crystalline layer, which was consistent with the fringe characteristics and nano-structures derived from HRTEM images. The reason may be that polycyclic aromatic compounds (PAHs) are the main products of incomplete combustion. As the surface growth of soot depends on the condensation of PAHs, this may cause the formation of amorphous carbon [72]. This direct experimental evidence could be valuable for refining soot surface growth models via PAH condensation.

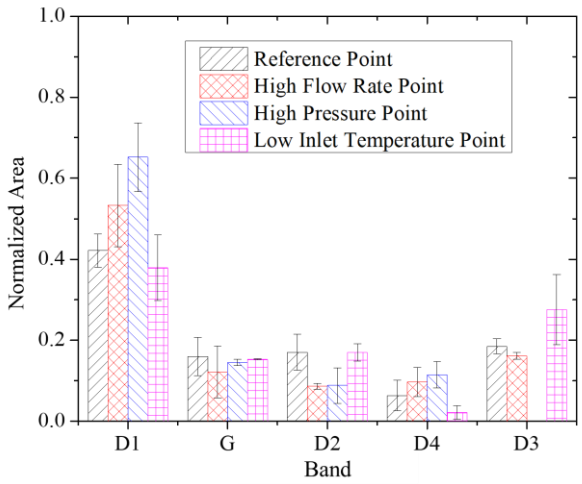

Figure 7. The area under each band normalized by the total area of all the bands from the fitted Raman spectra for different test points.

In addition to Raman intensity, the intensity ratios of the Raman bands can also be used to determine the order and the defects in soot particles with high sensitivity [62, 73]. The band intensity ratios of D1 and G, D2 and G, D3 and G were calculated and the results are shown in Figure 8.

In general, D1 represents a defect of graphite. The intensity ratio between D1 and G (I_{D1} / I_G) represents the graphite crystallinity of the soot which is the measure of defects in graphitic layers [74, 75]. As shown in Figure 8, the value from the High Flow Rate Point is the highest and that from the Low Inlet Temperature Point is the lowest, indicating that the high flow rate combustion generated soot particles of the highest graphite crystallinity while soot particles from the low inlet temperature condition have the highest amorphous content.

I_{D2} / I_G can be used as a relative measure of the surface area/volume ratio which is inversely proportional to the thickness of graphite crystallites [62]. In this study, the soot particles from the High Pressure Point give the lowest I_{D2} / I_G value and those from the Low Inlet Temperature Point are the highest. Thinner graphite crystallites tend to have more oxidation activity because the high

surface area could increase oxidation reactions on the graphene layer. The particles formed at the High Pressure Point have the most mature nanostructures with the least amorphous carbon content, as demonstrated by the lack of the D3 band in the Raman spectrum. Because of the lowest I_{D2} / I_G, the graphite crystals formed at this test point are the thickest, implying low oxidation and chemical activity. Compared to a Raman investigation on soot emissions from several commercial turbofan and turboshaft engines [71], this study shows the similar results on I_{D2}/I_G. We also estimated the fringe distance or the thickness of graphite crystallites from the HRTEM images. The average values and standard deviations of fringe distance are shown in Table 3. For the Reference Point, High Pressure Point, and High Flow rate Point, fringe distance is inversely proportional to I_{D2}/I_G, in agreement with the observation from Zhu et al. [59]. However, for the Low Inlet Temperature Point, the mean value of fringe distance is similar to that for the High Flow Rate Point, with the highest standard deviation. This discrepancy may be related to the difference in Raman linewidth and experimental uncertainty.

Table 3 The average values and standard deviations of fringe distance for the four points different condition points.

Condition Point	Reference Point	High Pressure Point	High Flow Rate Point	Low Inlet Temperature Point
Average value (nm)	0.23	0.30	0.45	0.45
Standard deviation (1σ) (nm)	0.04	0.03	0.08	0.09

The origin of the D3 band is related to amorphous carbon, and I_{D3} / I_G reflects the mass ratio of amorphous carbon to crystalline graphite [62, 73]. The soot particles formed at the Low Inlet Temperature Point are significantly different from those at the High Pressure Point with the lowest I_{D1} / I_G and the highest I_{D3} / I_G values. This may be due to the soot formation origins during insufficient combustion at the low inlet temperature. On the contrary, the I_{D3} / I_G value at the High Pressure Point is unmeasurable, in agreement with the results from the HRTEM measurements

that high combustion pressure enhances the formation of orderly graphitic contents in the soot particles.

The band width of D1 in full width at half maximum (FWHM) for each condition point is presented in Fig. 8. According to previous investigation, D1 FWHM is negatively correlated to chemical heterogeneity and crystal structure order [68]. In this study, at the High Pressure and High Flow Rate Points, both I_{D1} / I_G and D1 FWHM were higher than those at the Reference Point, indicating higher chemical heterogeneity and lower crystal structure, while those at the Low Inlet Temperature Point were lower, indicating lower chemical heterogeneity and higher crystal structure. However, the highest I_{D1} / I_G was at the High Flow Rate Point and the largest D1 FWHM was at the High Pressure Point. As discussed by Ferrari and Robertson [64], the broadening of the D peak is related to the distribution of carbon clusters with different orders and dimensions, and thus the information about the less distorted aromatic rings is in the intensity maximum rather than the width, which is affected by graphite disorder. It implies that at the High Pressure Point, chemical heterogeneity is more broadly distributed than that at the High Flow Rate Point.

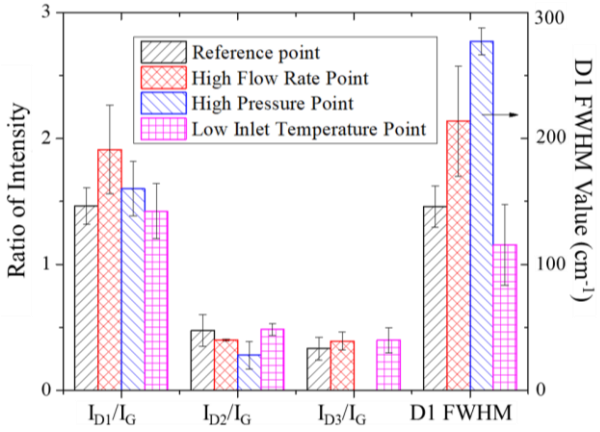

Figure 8. Relative intensity and the full width at half maximum (FWHM) of D1 obtained from Raman spectra.

4. Conclusion

The nanostructure and morphology of soot particles emitted from an accurately controlled combustion reactor simulating aero-engine combustors were investigated under different combustion pressures (1.2 bar vs 2.0 bar), inlet fuel flow rates (1.0 g/s vs 1.5 g/s), and inlet temperatures (360 °C vs 430 °C) at fuel-rich combustion with the equivalent ratio ϕ of 1.2. The main findings are obtained as follows:

1) Low combustion temperature decreases the size of primary soot particles with a low degree of graphitization, and their small fringe length and large fringe tortuosity indicate high oxidation reactivity for the soot particles.

2) High combustion pressure and high inlet flow rate can increase the size of the primary soot particles that causes less oxidation of soot particles. The nanostructure and morphology characteristics of the soot particles are highly related to the JSR operational parameters. The higher combustion pressure or lower inlet flow rate results in fringe length increase and fringe tortuosity decrease with more ordered graphene layer activity, whilst the lower combustion temperature favors the generation of the soot particles with amorphous structure possessing shorter fringe length and greater fringe tortuosity. The particles formed under the high combustion pressure have the most mature nanostructure with little amorphous carbon and a high degree of graphitization.

3) The primary soot particles in this study all exhibit 'shell-core' nanostructures with the graphitized outer shell and many inner cores, indicating more degree of graphitization and higher oxidation resistance. This type is significantly different from the types observed in primary particles of diesel engines exhausts, which upholds the conjecture that the discrepancy of combustion conditions between aero-engines and diesel engines would lead to a dramatic difference in terms of soot nano-structures and thus soot reactivity.

This study offers direct experimental evidences that different combustion conditions of an aero-

engine combustor can alter soot nano-structures and reactivity potential, which could be associated with the capability of soot acting as ice forming agents in contrail formation. The observation of this study might be crucial in the future for assessing the potential of mitigating climate impacts of aviation activities by reducing soot emissions and altering their nano-structures as well as their oxidation potential.

Supplementary Material

Table S1 shows the uncertainty analysis. The detailed information of fringe length and fringe tortuosity are shown in Table S2 and Table S3, respectively. Table S4 shows the spectroscopic origins of the bands of Raman spectra. It also gives detailed steps of post-processed HRTEM images using MATLAB-based coding.

Acknowledgment

Thanks to Professor Randy Vander Wal from Pennsylvania State University and Ömer L. Gülder from University of Toronto for constructive comments and helpful discussion. This work was mainly supported by the National Natural Science Foundation of China (51922019 & 51920105009). This work was partially supported by National Engineering Laboratory for Mobile Source Emission Control Technology (NELMS2018A02), Open Foundation of Beijing Key Laboratory of Occupational Safety and Health (2019), and China Scholarship Council (CSC number: 201906020042).

References

[1] Yim SHL, Lee GL, Lee IH, Allroggen F, Ashok A, Caiazzo F, et al. Global, regional and local health impacts of civil aviation emissions. Environmental Research Letters 2015;10(3):034001.

[2] Brunelle-Yeung E, Masek T, Rojo JJ, Levy JI, Arunachalam S, Miller SM, et al. Assessing the impact of aviation environmental policies on public health. Transport Policy 2014;34:21-8.

[3] https://www.icao.int/annual-report-2014/Pages/CH/progress-on-icaos-strategic-objectives-safety-environmental-protection-caep_CH.aspx; [accessed 7 May 2021]].
[4] Kärcher B, Yu F. Role of aircraft soot emissions in contrail formation. Geophysical Research Letters 2009;36(1).
[5] Archer-Nicholls S, Lowe D, Schultz DM, McFiggans G. Aerosol–radiation–cloud interactions in a regional coupled model: the effects of convective parameterisation and resolution. Atmos Chem Phys 2016;16(9):5573-94.
[6] Zhao B, Liou K-N, Gu Y, Li Q, Jiang JH, Su H, et al. Enhanced PM 2.5 pollution in China due to aerosol-cloud interactions. Scientific Reports 2017;7(1):4453.
[7] Kärcher B. Formation and radiative forcing of contrail cirrus. Nature Communications 2018;9(1):1824.
[8] Grimonprez S, Wu J, Faccinetto A, Gosselin S, Riber E, Cuenot B, et al. Hydrophilic properties of soot particles exposed to OH radicals: A possible new mechanism involved in the contrail formation. Proceedings of the Combustion Institute 2020.
[9] Vander Wal RL, Tomasek AJ. Soot oxidation: dependence upon initial nanostructure. Combustion and Flame 2003;134(1):1-9.
[10] Stanmore BR, Brilhac JF, Gilot P. The oxidation of soot: a review of experiments, mechanisms and models. Carbon 2001;39(15):2247-68.
[11] Ghiassi H, Toth P, Jaramillo IC, Lighty JS. Soot oxidation-induced fragmentation: Part 1: The relationship between soot nanostructure and oxidation-induced fragmentation. Combustion and Flame 2016;163:179-87.
[12] Yehliu K, Vander Wal RL, Armas O, Boehman AL. Impact of fuel formulation on the nanostructure and reactivity of diesel soot. Combustion and Flame 2012;159(12):3597-606.
[13] Qu L, Wang Z, Zhang J. Influence of waste cooking oil biodiesel on oxidation reactivity and nanostructure of particulate matter from diesel engine. Fuel 2016;181:389-95.
[14] Marhaba I, Ferry D, Laffon C, Regier TZ, Ouf F-X, Parent P. Aircraft and MiniCAST soot at the nanoscale. Combustion and Flame 2019;204:278-89.
[15] Song J, Song C, Tao Y, Lv G, Dong S. Diesel soot oxidation during the late combustion phase. Combustion and Flame 2011;158(3):446-51.
[16] An Y, Jaasim M, Vallinayagam R, Vedharaj S, Im HG, Johansson B. Numerical simulation of combustion and soot under partially premixed combustion of low-octane gasoline. Fuel 2018;211:420-31.
[17] Huang C-H, Vander Wal RL. Effect of soot structure evolution from commercial jet engine burning petroleum based JP-8 and synthetic HRJ and FT fuels. Energy & Fuels 2013;27(8):4946-58.
[18] Liati A, Brem BT, Durdina L, Vögtli M, Arroyo Rojas Dasilva Y, Dimopoulos Eggenschwiler P, et al. Electron microscopic study of soot particulate matter emissions from aircraft turbine engines. Environmental science & technology 2014;48(18):10975-83.
[19] Liati A, Schreiber D, Alpert PA, Liao Y, Brem BT, Corral Arroyo P, et al. Aircraft soot from conventional fuels and biofuels during ground idle and climb-out conditions: Electron microscopy and X-ray micro-spectroscopy. Environmental Pollution 2019;247:658-67.
[20] Rutar Shuman T. NOx and CO formation for lean-premixed methane-air combustion in a jet-stirred reactor operated at elevated pressure. 2010.
[21] Barari G, Popolan-Vaida D, Vasu S. Pyrolysis of RP-2 and Surrogate Fuels in a Jet Stirred Reactor Coupled with Synchrotron Photo Ionization Mass Spectrometry. *55th AIAA Aerospace Sciences Meeting.* 2017:0612.

[22] Manzello SL, Lenhert DB, Stroud CB, Tsang W. The effects of aromatic species on soot particle size distribution and species concentration in a well stirred reactor/plug flow reactor. Fuel 2007;2(2):N2.
[23] Liati A, Brem BT, Durdina L, Vögtli M, Arroyo Rojas Dasilva Y, Dimopoulos Eggenschwiler P, et al. Electron Microscopic Study of Soot Particulate Matter Emissions from Aircraft Turbine Engines. Environmental Science & Technology 2014;48(18):10975-83.
[24] Russo C, Ciajolo A. Effect of the flame environment on soot nanostructure inferred by Raman spectroscopy at different excitation wavelengths. Combustion and Flame 2015;162(6):2431-41.
[25] Commodo M, Joo PH, De Falco G, Minutolo P, D'Anna A, Gülder ÖL. Raman Spectroscopy of Soot Sampled in High-Pressure Diffusion Flames. Energy & Fuels 2017;31(9):10158-64.
[26] Lespade P, Al-Jishi R, Dresselhaus MJC. Model for Raman scattering from incompletely graphitized carbons. 1982;20(5):427-31.
[27] Nemanich RJ, Solin SJPRB. First-and second-order Raman scattering from finite-size crystals of graphite. 1979;20(2):392.
[28] Tuinstra F, Koenig JL. Raman Spectrum of Graphite. 1970;53:1126.
[29] Song J, Alam M, Boehman AL, Kim U. Examination of the oxidation behavior of biodiesel soot. Combustion and Flame 2006;146(4):589-604.
[30] Xue X, Lin Y, Zhang C, Tian Y, Sung C-J. Experimental Study on NOx and CO Emissions of Aviation Kerosene and Coal-to-Liquid Synthetic Aviation Fuel in a Jet Stirred Combustion Reactor. 2014(45691):V04BTA003.
[31] Mao Y, Yu L, Wu Z, Tao W, Wang S, Ruan C, et al. Experimental and kinetic modeling study of ignition characteristics of RP-3 kerosene over low-to-high temperature ranges in a heated rapid compression machine and a heated shock tube. Combustion and Flame 2019;203:157-69.
[32] Zhang C, Hui X, Lin Y, Sung C-J. Recent development in studies of alternative jet fuel combustion: Progress, challenges, and opportunities. Renewable and Sustainable Energy Reviews 2016;54:120-38.
[33] Anderson B, Beyersdorf A, Hudgins C, Plant J, Thornhill K, Winstead E, et al. Alternative aviation fuel experiment (AAFEX). 2011;217059:408.
[34] Lobo P, Christie S, Khandelwal B, Blakey SG, Raper DW. Evaluation of Non-volatile Particulate Matter Emission Characteristics of an Aircraft Auxiliary Power Unit with Varying Alternative Jet Fuel Blend Ratios. Energy & Fuels 2015;29(11):7705-11.
[35] Brem BT, Durdina L, Siegerist F, Beyerle P, Bruderer K, Rindlisbacher T, et al. Effects of Fuel Aromatic Content on Nonvolatile Particulate Emissions of an In-Production Aircraft Gas Turbine. Environmental Science & Technology 2015;49(22):13149-57.
[36] Aizawa T, Nishigai H, Kondo K, Yamaguchi T, Nerva J-G, Genzale C, et al. Transmission Electron Microscopy of Soot Particles Directly Sampled in Diesel Spray Flame - A Comparison between US#2 and Biodiesel Soot. SAE International Journal of Fuels and Lubricants 2012;5(2):665-73.
[37] Schneider CA, Rasband WS, Eliceiri KW. NIH Image to ImageJ: 25 years of image analysis. Nature Methods 2012;9(7):671-5.
[38] Yehliu K, Vander Wal RL, Boehman AL. Development of an HRTEM image analysis method to quantify carbon nanostructure. Combustion and Flame 2011;158(9):1837-51.
[39] Apicella B, Ciajolo A, Tregrossi A, Abrahamson J, Vander Wal RL, Russo C. HRTEM and EELS investigations of flame-formed soot nanostructure. Fuel 2018;225:218-24.
[40] Chen L, Hu X, Wang J, Yu Y. Impacts of Alternative Fuels on Morphological and Nanostructural Characteristics of Soot Emissions from an Aviation Piston Engine. Environmental Science & Technology 2019.

[41] Stone R. Introduction to internal combustion engines. 1999.
[42] Dagaut P, Cathonnet M. The ignition, oxidation, and combustion of kerosene: A review of experimental and kinetic modeling. Progress in energy and combustion science 2006;32(1):48-92.
[43] Chen L, Liang Z, Zhang X, Shuai S. Characterizing particulate matter emissions from GDI and PFI vehicles under transient and cold start conditions. Fuel 2017;189:131-40.
[44] Ma Y, Zhu M, Zhang D. Effect of a homogeneous combustion catalyst on the characteristics of diesel soot emitted from a compression ignition engine. Applied Energy 2014;113:751-7.
[45] Jaramillo IC, Gaddam CK, Vander Wal RL, Lighty JS. Effect of nanostructure, oxidative pressure and extent of oxidation on model carbon reactivity. Combustion and Flame 2015;162(5):1848-56.
[46] Botero ML, Sheng Y, Akroyd J, Martin J, Dreyer JAH, Yang W, et al. Internal structure of soot particles in a diffusion flame. Carbon 2019;141:635-42.
[47] Botero ML, Chen D, González-Calera S, Jefferson D, Kraft M. HRTEM evaluation of soot particles produced by the non-premixed combustion of liquid fuels. Carbon 2016;96:459-73.
[48] Gaddam CK, Huang C-H, Vander Wal RL. Quantification of nano-scale carbon structure by HRTEM and lattice fringe analysis. Pattern Recognition Letters 2016;76:90-7.
[49] Li Z, Qiu L, Cheng X, Li Y, Wu H. The evolution of soot morphology and nanostructure in laminar diffusion flame of surrogate fuels for diesel. Fuel 2018;211:517-28.
[50] Zhang Y, Zhang R, Rao L, Kim D, Kook S. The influence of a large methyl ester on in-flame soot particle structures in a small-bore diesel engine. Fuel 2017;194:423-35.
[51] Zhou JH, Cheung CS, Zhao WZ, Ning Z, Leung CW. Impact of intake hydrogen enrichment on morphology, structure and oxidation reactivity of diesel particulate. Applied Energy 2015;160:442-55.
[52] Zhang Y, Zhang R, Rao L, Kook S. A Comparison between In-Flame and Exhaust Soot Nanostructures in a Light-Duty Diesel Engine. SAE Technical Paper; 2017.
[53] Toth P, Palotas AB, Ring TA, Eddings EG, Vander Wal R, Lighty JS. The effect of oxidation pressure on the equilibrium nanostructure of soot particles. Combustion and Flame 2015;162(6):2422-30.
[54] Vander Wal RL. A TEM Methodology for the Study of Soot Particle Structure. Combustion Science and Technology 1997;126(1-6):333-51.
[55] Ishiguro T, Takatori Y, Akihama K. Microstructure of diesel soot particles probed by electron microscopy: First observation of inner core and outer shell. Combustion and Flame 1997;108(1):231-4.
[56] Zhang R, Kook S. Structural evolution of soot particles during diesel combustion in a single-cylinder light-duty engine. Combustion & Flame 2015;162(6):2720-8.
[57] Wang Y, Liang X, Tang G, Chen Y, Dong L, Shu G. Impact of lubricating oil combustion on nanostructure, composition and graphitization of diesel particles. Fuel 2017;190:237-44.
[58] Verma P, Pickering E, Jafari M, Guo Y, Stevanovic S, Fernando JFS, et al. Influence of fuel-oxygen content on morphology and nanostructure of soot particles. Combustion and Flame 2019;205:206-19.
[59] Zhu L, Xiao Y, Cheung CS, Guan C, Huang Z. Combustion, gaseous and particulate emission of a diesel engine fueled with n-pentanol (C5 alcohol) blended with waste cooking oil biodiesel. Applied Thermal Engineering 2016;102:73-9.
[60] Ye P, Sun C, Lapuerta M, Agudelo J, Vander Wal R, Boehman AL, et al. Impact of rail pressure and biodiesel fueling on the particulate morphology and soot nanostructures from a common-rail turbocharged direct injection diesel engine. International Journal of Engine Research 2014;17(2):193-208.

[61] Xiao M, Liu H, Bi X, Wang H, Lee C-fF. Experimental and Numerical Investigation on Soot Behavior of Soybean Biodiesel under Ambient Oxygen Dilution in Conventional and Low-Temperature Flames. Energy & Fuels 2014;28(4):2663-76.
[62] Sadezky A, Muckenhuber H, Grothe H, Niessner R, Pöschl U. Raman microspectroscopy of soot and related carbonaceous materials: Spectral analysis and structural information. Carbon 2005;43(8):1731-42.
[63] Schmid J, Grob B, Niessner R, Ivleva NP. Multiwavelength Raman Microspectroscopy for Rapid Prediction of Soot Oxidation Reactivity. Analytical Chemistry 2011;83(4):1173-9.
[64] Ferrari AC, Robertson J. Interpretation of Raman spectra of disordered and amorphous carbon. Physical Review B 2000;61(20):14095-107.
[65] Lapuerta M, Oliva F, Agudelo JR, Stitt JP. Optimization of Raman Spectroscopy Parameters for Characterizing Soot from Different Diesel Fuels. Combustion Science and Technology 2011;183(11):1203-20.
[66] Wang Y, Alsmeyer DC, McCreery RLJCoM. Raman spectroscopy of carbon materials: structural basis of observed spectra. 1990;2(5):557-63.
[67] Ivleva NP, Messerer A, Yang X, Niessner R, Pöschl U. Raman Microspectroscopic Analysis of Changes in the Chemical Structure and Reactivity of Soot in a Diesel Exhaust Aftertreatment Model System. Environmental Science & Technology 2007;41(10):3702-7.
[68] Dippel B, Jander H, Heintzenberg JJPCCP. NIR FT Raman spectroscopic study of flame soot. 1999;1(20):4707-12.
[69] Bacsa WS, Lannin JS, Pappas DL, Cuomo JJ. Raman scattering of laser-deposited amorphous carbon. Physical Review B Condensed Matter 1993;47(16):10931-4.
[70] Shirakawa H, Ito T, Ikeda S. Raman Scattering and Electronic Spectra of Poly(acetylene). Polymer Journal 1973;4(4):460-2.
[71] Saffaripour M, Tay L-L, Thomson KA, Smallwood GJ, Brem BT, Durdina L, et al. Raman spectroscopy and TEM characterization of solid particulate matter emitted from soot generators and aircraft turbine engines. Aerosol Science and Technology 2017;51(4):518-31.
[72] Mao Q, van Duin ACT, Luo KH. Formation of incipient soot particles from polycyclic aromatic hydrocarbons: A ReaxFF molecular dynamics study. Carbon 2017;121:380-8.
[73] Parent P, Laffon C, Marhaba I, Ferry D, Regier TZ, Ortega IK, et al. Nanoscale characterization of aircraft soot: A high-resolution transmission electron microscopy, Raman spectroscopy, X-ray photoelectron and near-edge X-ray absorption spectroscopy study. Carbon 2016;101:86-100.
[74] Agudelo JR, Álvarez A, Armas O. Impact of crude vegetable oils on the oxidation reactivity and nanostructure of diesel particulate matter. Combustion and Flame 2014;161(11):2904-15.
[75] Vander Wal RL. Soot nanostructure: Definition, quantification and implications. SAE Technical Paper; 2005.